International Journal of Impact Engineering 178 (2023) 104593

Contents lists available at ScienceDirect

International Journal of Impact Engineering

journal homepage: www.elsevier.com/locate/ijimpeng

Critical assessment and demonstration of high-emissivity coatings for improved infrared signal quality for Taylor–Quinney coefficient experimentation

Seyyed-Danial Salehi, Owen Kingstedt *

Department of Mechanical Engineering, University of Utah, Salt Lake City, UT, 84112, United States

ARTICLE INFO

Keywords:
Taylor–Quinney coefficient measurement
Split-Hopkinson pressure bar
Transfer matrix method
Infra-red thermography
High strain rate deformation

ABSTRACT

Over the infrared (IR) spectrum metals have relatively low emissivity. Considering that modern studies focused on determining the Taylor–Quinney coefficient rely on IR-based measurements to quantify temperature rise, there is a need to improve measurement certainty. This is of particular concern during the earliest stages of deformation when small temperature rises result in a low IR-signal to noise ratio. Herein an economical approach to improving signal quality is presented based on the deposition of a thin high emissivity coating on the material substrate (i.e., specimen) of interest. Coating material and coating thickness selection are founded on both heat transfer and electromagnetic performance. A maximum allowable thickness of 1 μm was determined for the coating to ensure the recorded temperature of the coating closely matches the temperature of the deforming substrate (i.e., specimen) during the sub-millisecond duration of a split-Hopkinson (or Kolsky) pressure bar experiment. Using the transfer matrix method, the spectral emissivity of coatings made from commonly available metallic deposition sources with increasing thicknesses was calculated. Theoretical predictions identified a 250 nm thick Ti coating as a promising candidate for increasing surface emissivity without the coating acting as a thermal barrier. Confirmation of the coating layer's ability to substantially improve IR signal amplitudes was examined experimentally for two low emissivity materials, specifically OFHC copper (Cu) and Magnesium (Mg) alloy AZ31B. IR detector calibration experiments showed a four to six times improvement in signal amplitude compared to native Cu and Mg surfaces. Additionally, the calibration curves of coated specimens converge exhibiting the same behavior allowing for a unified calibration curve to be used regardless of substrate material. Split-Hopkinson pressure bar experiments supported by IR thermography were conducted on coated specimens and Taylor–Quinney coefficients are reported. Taylor–Quinney coefficients obtained, are compared to literature values when appropriate, and show positive agreement to previously reported values. Real-time high-speed imaging and post-mortem analysis showed robust adhesion between the substrate to the thin Ti layer up to 16% strain.

1. Introduction

Deforming crystalline metallic solids store a portion of their strain energy through defects such as dislocations, deformation twins, and residual strains [1–5]. The remainder of this energy is converted to heat. The efficiency of the conversion of plastic work (or power) to heat is commonly referred to as the Taylor–Quinney or β coefficient. It is of crucial importance to have a thorough understanding of the Taylor–Quinney coefficient when developing temperature-dependent constitutive models that are used to predict macroscopic stress strain behavior [6–9] and the onset of thermoplastic instabilities [10,11] such as adiabatic shear band formation. Additionally, if the temperature rise occurring during deformation is significant (high β) and thermal softening is considerable, failure modes may be altered [12–14]. Specific applications where the interplay of self heating and thermal softening are of interest include high speed machining, ballistic performance, metal forming, and vehicle crash.

Based on the pioneering work of Taylor and co-workers [2], the Taylor–Quinney coefficient is commonly assumed to be $\beta = 0.9$, a 90% efficiency when converting the work of deformation to heat, regardless of material. Modern experimental efforts have shown that this constant conversion efficiency assumption to be an oversimplification whereas several factors such as strain [3,15,16], strain rate [16,17],

* Corresponding author.
E-mail address: o.kingstedt@utah.edu (O. Kingstedt).

https://doi.org/10.1016/j.ijimpeng.2023.104593
Received 11 August 2022; Received in revised form 14 March 2023; Accepted 28 March 2023
Available online 10 April 2023

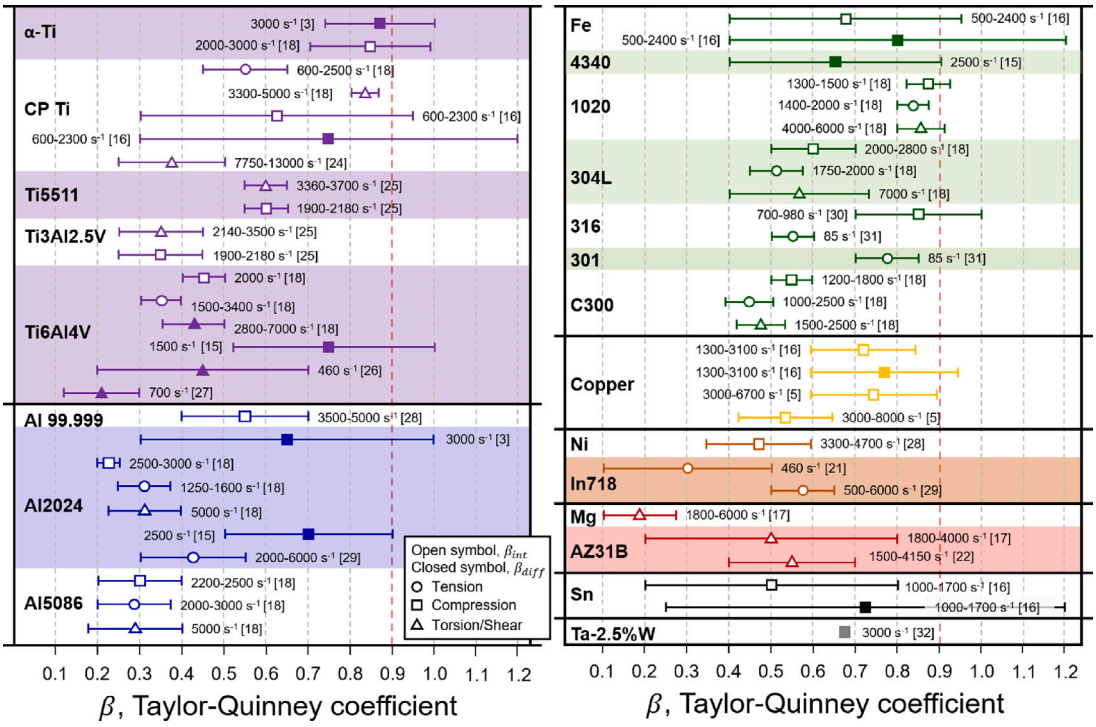

Fig. 1. A summary of recently reported Taylor–Quinney coefficients of metallic systems measured using non-contact techniques under adiabatic conditions at dynamic strain rates [3,5,15–18,21,22,24–32]. The red vertical dashed line at 0.9 represents the commonly used approximation of the Taylor–Quinney factor.

loading mode [18], grain size [19–21], and active deformation mechanisms [22] strongly affect reported Taylor–Quinney coefficients. Two versions of the Taylor–Quinney coefficient are reported in literature, the conversion of plastic power to heat generation rate (β_{diff}), and the conversion of plastic work to heat (β_{int}) [23]. Due to thermodynamic restrictions, β_{int} is always inferior to one unless a latent heat source (e.g., phase transformation) is present during deformation. Alternatively, β_{diff} has no such restrictions. Fig. 1 presents a summary of experimentally measured Taylor–Quinney coefficients for a variety of metallic material systems. Studies included in Fig. 1 are limited to those that utilized non-contact temperature measurements (e.g., pyrometry) and used high-strain rate experimental techniques to achieve adiabatic loading conditions. Strain rates, loading configuration, and the span of the selected Taylor–Quinney coefficient value (β_{int} vs. β_{diff}) observed during plastic strain accumulation are reported. Additional details pertaining to material condition, microstructure, and temperature measurement techniques can be found in the respective reference.

Experimental measurement of the Taylor–Quinney coefficient requires the synchronized recording of stress, strain, and temperature rise. This requirement is frequently accomplished using a split-Hopkinson pressure bar (SHPB) along with non-contact infrared (IR) thermography. Two prominent optical configurations utilized for non-contact IR thermography include the Newtonian optical system [17,33,34] and double-Schwarzschild optical system [35–37]. Once the optical system is built and aligned the output of the IR detector is solely a function of the interrogated sample's emissivity and temperature. Although IR detectors have high responsivity, the emissivity of metals tends to be low over the IR range. Careful optical system alignment and calibration is necessary to convert IR detector voltage outputs to temperature. As is shown in Fig. 1, there is considerable lab-to-lab and material-to-material variation in reported Taylor–Quinney coefficients. The most critical step in the reduction of data during post-processing of Taylor–Quinney coefficient experiments is the assignment of calibration curves that convert detector outputs to temperature. Slight variations in the calibration curve can result in dramatically different reported values. Additionally, identifying calibration curves at temperatures close to ambient is challenging due to signal amplitudes being close to the IR detector noise floor. The goal of the presented work is to propose a solution to the low emissivity exhibited by metals, with the objective of improving signal quality thereby making calibration curves less susceptible to noise contamination and to improve near room temperature measurement.

The use of coatings to tailor surface emissivity has received significant attention from radiative cooling [38] to spacecraft applications [39,40]. E-beam evaporation [39], micro-arc oxidation [41,42], physical vapor deposition [40], chemical vapor deposition [43] can be utilized to create a high emissivity surface coating. These methods are difficult to translate to Taylor–Quinney coefficient studies. Mechanically, any applied high-emissivity coatings must have robust adhesion, deform freely with the underlying substrate without exhibiting catastrophic failure for at least one loading cycle, and must not be susceptible to inertial effects during high strain rate deformation. Optically, the coating must exhibit a constant emissivity ensuring that thickness changes during plastic deformation do not alter its performance. Additionally, the coating must be thin enough such that heat transfer through the coating thickness occurs over the short duration of a SHPB experiment ensuring that coating surface measurements closely match those of the deforming substrate. These challenges are investigated theoretically and experimentally in the presented work.

2. Methodology

2.1. Coating Design — Optical performance over the IR spectrum

The electromagnetic waves emitted by a medium are a function of temperature, emissivity, and wavelength of the incident radiation. As temperature and emissivity increase, total emissive power increases. This physical property of materials, allows the measurement of temperature rise using non-contact IR detectors (e.g., MCT or InSb element arrays, infrared cameras). As an electromagnetic wave interacts with a medium, a portion of the wave is reflected, a portion is absorbed,

Fig. 2. Schematic of the TMM algorithm to predict the emissivity.

and the remainder is transmitted through the medium. For normal incident radiation, an estimate of surface reflectivity (R) can be obtained according to Fresnel's formula, presented in Eq. (1),

$$R = \frac{(n-1)^2 + k^2}{(n+1)^2 + k^2} \tag{1}$$

where, n and k are the refractive index and extinction coefficient, respectively. Assuming a uniform isotropic opaque material in thermal equilibrium, surface emissivity (ϵ) is related to surface reflectivity (R), through $\epsilon = 1 - R$. The extinction coefficient (k) for most metals is high over the IR range, with Cu and Mg having values of 63 [44] and 43.2 [45] at a wavelength of 10 μm, respectively. The refractive indexes for Cu and Mg, also at a wavelength of 10 μm, are 8.31 [44] and 21.3 [45], respectively. Thus, their reflectivity approaches one and their emissivity trends towards small values (e.g., $\epsilon = 0.008$ for Cu and $\epsilon = 0.036$ for Mg). As a direct consequence of low material emissivity, captured IR signals, particularly those obtained at the earliest stages of plasticity during an IR thermography experiment or those associated with deformation heterogeneities are challenging to interpret.

There are multiple approaches to improving IR signal amplitude. These include optimizing optical system parameters to maximize emissive power received by the IR detector [37], increasing a material's emissivity through greater surface roughness [38,46], modifying surface texture [47] or adding periodic surface features [48]. Assuming an appropriately designed optical system is used, surface modifications that improve emissivity that do not impact mechanical or physical behavior should be considered. Doping is not considered as the primary motivation of thermo-mechanics studies to characterize base alloy performance. It is well known that during plastic deformation surface roughness is altered. Therefore, modifications that add designed surface texture or periodic features that would randomly change as a result of the surface roughening occurring during plastic deformation are not considered. In addition, creating textured surfaces or designed periodic features involves multiple processing steps and thus is not an economic method to increase emissivity. Having considered the aforementioned mechanical, optical, and heat transfer requirements, depositing a thin coating layer of a high emissivity material presents as a straightforward method to increase the emissivity of the sample.

The Transfer Matrix Method (TMM) was implemented to obtain the emissivity of a two layer metallic system comprised of a thin film coating on substrate [49–51]. The TMM code generated was validated against the absorption results reported for Metal–Insulator–Metal Fabry–Perot structures in Ref. [49] (see supplementary data). The TMM code calculates the global scattering matrix of the layered system. The mode coefficients of the transmitted and reflected waves are obtained from the multiplication of the incident wave mode and the global scattering matrix. Finally the reflected and transmitted electromagnetic fields are acquired [51]. The schematic of the TMM algorithm to predict the emissivity is described in Fig. 2. The two layer metallic system was modeled to have a Cu or Mg substrate with various metal coatings. Cu and Mg were chosen as substrate materials due to: (1) their low emissivity; (2) Cu's high ductility and favorable homogeneous deformation; (3) the existence of previous Cu Taylor–Quinney coefficient studies which can be used to confirm measurement accuracy; and (4) to the authors' knowledge the Taylor–Quinney coefficient of Mg AZ31B obtained under dynamic tension has yet to be reported.

The simulated coating materials were selected based on commonly available deposition sources (e.g., Ti, W, Cr, Mg, Au, Ag). Refractive index (n) and extinction coefficient (k) values for different metals were extracted from Refs. [44,45,52]. The spectral radiance of the two layer system was obtained using Planck's formula presented in Eq. (2),

$$B_\lambda(\lambda, T) = \frac{2hc^2}{\lambda^5} \frac{1}{e^{\frac{hc}{\lambda k_B T}} - 1}. \tag{2}$$

In Planck's formula h, c, λ, k_B, and T are Planck's constant (6.62×10^{-34} m^2 kg/s, speed of light (3×10^9 m/s), wavelength, Boltzmann constant's (1.38×10^{-23} m^2 kgs^{-2}K^{-1}), and temperature, respectively. The responsivity of the liquid nitrogen cooled MCT (HgCdTe) IR detector (MCT-13-0.10) was provided by its manufacturer (i.e., IR Associates) as a function of wavelength. Fig. 3(a) shows the normalized radiance of a blackbody at room temperature as a function of wavelength while Fig. 3(b) presents the responsivity of the IR detector (Infrared Associates, LN2 cooled MCT-13-0.10) as a function of wavelength.

Once the emissivity of the two layer system was calculated, an estimate of the IR detector output can be predicted using Eq. (3). Note this estimate of the IR detector output is primarily useful in providing the proportional difference between material coating emissivity, but is unable to provide an exact IR detector output voltage. In Eq. (3), $B(\lambda)$ is the sample's radiance (e.g., as shown in Fig. 3(a)), ϵ is the sample's emissivity, λ_1 and λ_2 denote the start and end of the wavelength spectrum to which the detector is sensitive (2 μm and 15 μm, respectively), $\chi(\lambda)$ is a weighting function dictated by the spectral sensitivity of the IR detector (see Fig. 3(b)), and C_0 is a constant dependent on the efficiency and alignment of the optical system used.

$$\zeta(T) = C_0 \int_{\lambda_1}^{\lambda_2} B(T, \lambda)\epsilon(\lambda)\chi(\lambda)\, d\lambda \tag{3}$$

Using the TMM, the spectral emissivity of selected deposition coatings, and the IR detector sensitivity, the emissivity of the two layer system was determined. Fig. 4(a) shows the evolution of emissivity of a variety of coatings as a function of thickness on a Cu substrate. For each coating material it can be seen that an optimal thickness for achieving an opaque coating exists, after which increased deposition thicknesses exhibit limited increases in emissivity. Among the material coatings investigated, Titanium (Ti) was found to have the highest emissivity considering the spectral sensitivity of the IR system (see Fig. 4(b)). For this reason, Ti was selected as the candidate coating material for further investigation. An additional point of consideration when selecting the coating material is the deposition thickness required to achieve opacity. A final coating thickness of 250 nm is desirable, as greater deposition thicknesses can be susceptible to failure. Failure can be driven by the presence of high residual stresses induced during deposition as a result of differences in coefficients of thermal expansion or lattice spacing of the film and substrate material. If the stresses experienced by the film are sufficient, premature failure can occur through surface delamination which can lead to complete film delamination from the surface or through localized regions of the film breaking up via cracking. Furthermore, the rapid acceleration the specimen and film experience during an Hopkinson bar experiment are amenable to thinner films as inertial effects could also drive undesirable failure of the film.

2.2. Coating Design — Heat transfer performance

A primary consideration when adding a surface coating to a substrate is understanding the circumstances under which the coating material matches the thermal state of the substrate whose temperature

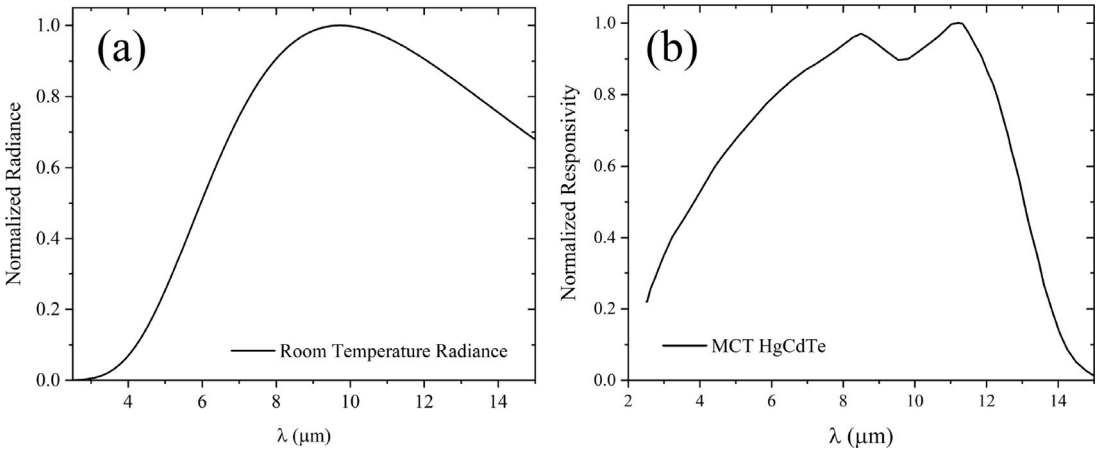

Fig. 3. (a) Normalized radiance of a blackbody at room temperature (25 °C) as a function of wavelength and (b) the normalized responsivity of the MCT IR detector as a function of wavelength.

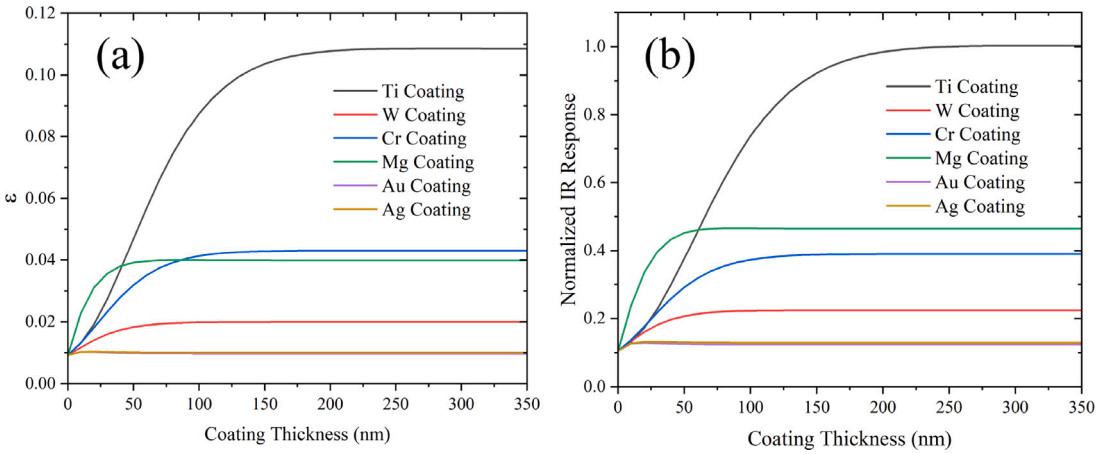

Fig. 4. (a) Change in emissivity of a copper substrate with various coatings as a function of coating thickness and (b) estimated normalized response of the IR detector as a function of coating thickness showing the proportional differences among coating thicknesses simulated using TMM.

evolves during deformation. The transient heat conduction equation, presented below, governs the temperature evolution of the substrate (and coating) during deformation. Multiple assumptions and restrictions are considered in Eq. (4) and the complete derivation is presented in [53],

$$\rho c_p \dot{T} = K_0 \nabla^2 T - \gamma T_0 \frac{E_{spec}}{1-2\nu} \dot{\epsilon}^e_{kk} + \beta_{diff} \sigma_{ij} \dot{\epsilon}^p_{ij}. \tag{4}$$

In the transient heat conduction equation, γ, c_p, K_0, and ν are the coefficient of thermal expansion, heat capacity, thermal conductivity, and Poisson's ratio, respectively. β_{diff} is the rate at which the plastic power is being converted to heat, and $\dot{\epsilon}^e_{kk}$, $\dot{\epsilon}^p_{ij}$ are the elastic and plastic strain-rates.

In light of experimental considerations a number of simplifications are applied to Eq. (4). First, thermo-elastic effects are considered to be negligible due to previous studies finding them to be small ($\approx$ 0.2 °C [4]) compared to the temperature rise due to thermoplastic effects. Therefore, the second term on the right is approximated as zero. Next, heat conduction along the longitudinal and transverse directions is neglected because of the existence of adiabatic conditions and uniformity of properties along these two in-plane directions. The presence of adiabatic conditions during an experiment can be confirmed when the Fourier number (F_o) is less than 0.01 [54]. The Fourier number, $F_o = \alpha t / l^2$, was calculated and found to be less than 0.01 for both Cu and Mg substrates where α is thermal diffusivity (1.13×10^{-4} for Cu, 9×10^{-6} for Ti), l in this case is the specimen gauge length (15.24 mm), and t is the experiment (or loading) duration (800 μs). In addition to the Fourier number analysis, in-depth analysis was conducted using the formulation presented in by Hodowany et al. [3] to obtain the temperature distribution in the sample during the Kolsky bar experiment. According to this heat conduction analysis, the heat loss over 90% of the sample's gauge length remains below 1%, and only small regions in the vicinity of the bars experience a temperature drop. IR thermography measurements are restricted to the central region of the gauge section. Thus it is expected that temperature measurements made are representative of the deforming material under adiabatic conditions. Thermal conductivity is limited to occurring through the thickness of the coating material and not within the plane of the specimen due to the order of magnitude difference in lengthscales of the gauge section length and width (millimeters) compared to the coating thickness (microns) and the short experiment duration. Nominal specimen dimensions are presented in Fig. 6. Lastly, during uniform deformation (i.e., pre-necking) it is assumed that heat generated is uniform throughout the gauge section. Therefore, the final heat conduction equations that represent a

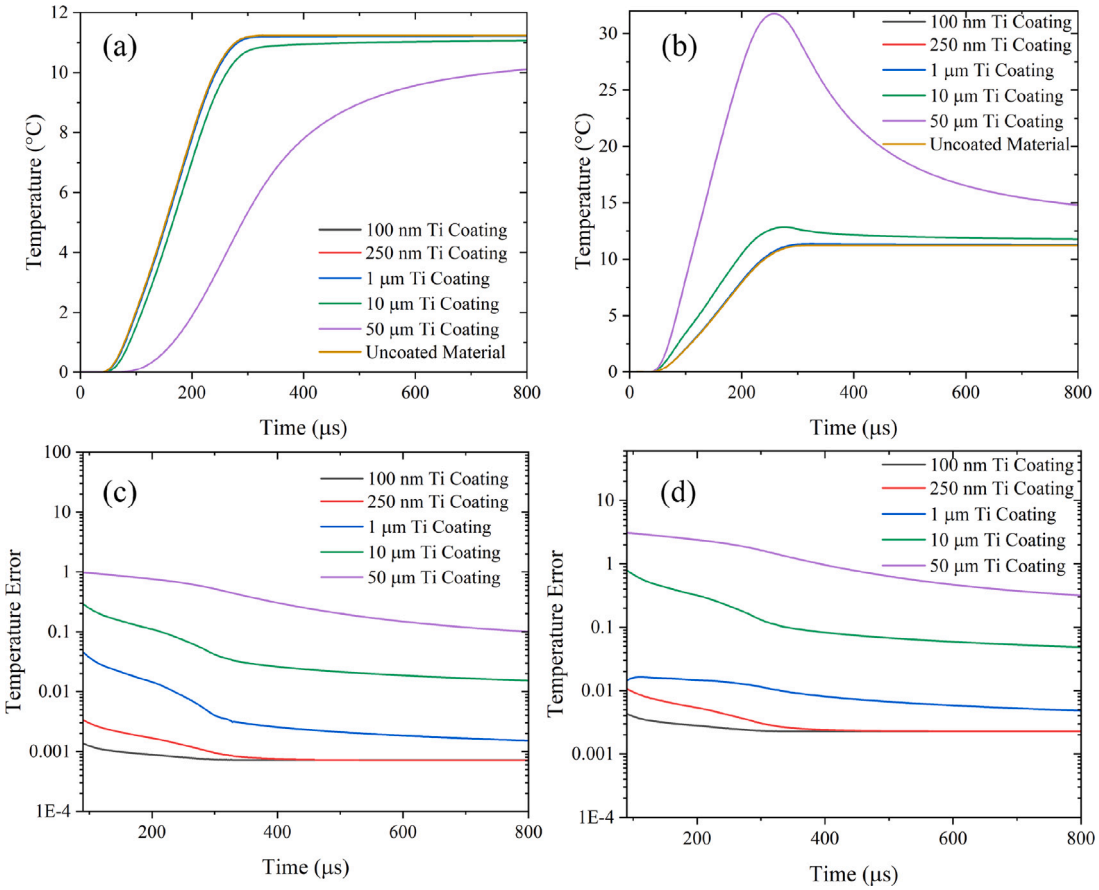

Fig. 5. Simulation of the effect of coating thickness and substrate vs. coating heat generation on observed surface temperature. (a) Case of heat generation limited to the substrate ($\beta_{diff},s = 0.9$) with not heat generation in coating ($\beta_{diff},c = 0$). (b) Case of heat generation in coating significantly exceeding that of the substrate ($\beta_{diff},c = 3\beta_{diff},s$). (c) Temperature error (Error $= |T_s - T_c|/T_s$) of the case shown in (a). (d) Temperature error of case shown in (b).

deforming substrate and coating are as follows:

$$\begin{aligned}
\rho_s c_{p,s}\dot{T}_s &= K_{0,s}\frac{\partial^2 T_s}{\partial z^2} + \beta_{diff,s}\dot{W}_{p,s},\\
\rho_c c_{p,c}\dot{T}_c &= K_{0,c}\frac{\partial^2 T_c}{\partial z^2} + \beta_{diff,c}\dot{W}_{p,c},\\
\frac{\partial T_s(0,t)}{\partial z} = 0,\ \frac{\partial T_s(l_s,t)}{\partial z} &= -\frac{\partial T_c(0,t)}{\partial z},\\
T_s(l_s,t) = T_c(0,t),\ \frac{\partial T_c(l_c,t)}{\partial z} &= 0,\\
T_s(z,0) = T_c(z,0) &= 0.
\end{aligned} \tag{5}$$

In this set of equations, the s and c subscripts denote the substrate and coating, l_s and l_c are the thickness of substrate and coating respectively. The first two equations are the transient heat conduction equations for the substrate and coating, respectively. The third and fourth row of equations are the insulated boundary conditions at the free surfaces and continuity of the temperature and heat flux at the interface between the coating and the substrate, respectively. The fifth row of equations are the initial conditions where both the substrate and coating have zero initial temperature. The temperature evolution of the coating was solved using finite element modeling in Abaqus software using 20 node quadratic brick elements. Material specific constants used in the simulations are presented in Table 1.

The time dependent temperature evolution of the coating was modeled over 800 μs to match the duration of a traditional SHPB experiment. SHPB experiments are described in detail in a subsequent section. Two extreme cases were modeled for coating thicknesses of 100 nm, 250 nm, 500 nm, 1 μm, 10 μm, and 50 μm. The first case examines the scenario where heat generation (i.e., temperature rise) is restricted to occurring only in the substrate ($\beta_{diff} > 0$) and no heat is generated by the coating ($\beta_{diff} = 0$). In this scenario the substrate acts as a heat source and the coating acts as a heat sink whose temperature evolution is dictated by through thickness conduction. The second case examined has the coating material generating heat at a rate that is three times greater than the substrate ($\beta_{diff,c} = 3\beta_{diff,s}$). In this second case the substrate acts as the heat sink and the coating as the heat source. For both cases, the substrate β_{diff},s was considered to be 0.9 due to this being a commonly utilized value when approximating the Taylor–Quinney coefficient in simulations. Results of the first simulation case are provided in Fig. 5(a), and for the second case in Fig. 5(b). For each case the temperature error defines as the absolute temperature difference between the substrate and the coating normalized by the substrate temperature (Error $= |T_s - T_c|/T_s$) is presented in Fig. 5(c) and 5(d), respectively. For the two extreme cases considered it is evident that as the coating thickness increases it acts a thermal barrier (case one) or misrepresents the substrate temperature (case two). At thicknesses of a micron or less, temperature error reduces with increasing time. Over the earliest stages of deformation, the temperature error for sub micron thicknesses decays from 10% to less than 1%. Considering the temperature state of the substrate (or coating) is less than 2 °C, the temperature error is on the order of the temperature associated with

Table 1
Material constants used in simulations.

	Density (kg/m^3)	Specific heat (J/kg°C)	Thermal conductivity (W/m°C)
Copper citation [55]	8960	380	386
Titanium citation [56]	4500	540	22

thermo-elastic effects. As stated previously, in many thermo-mechanics studies thermo-elastic effects are considered to be negligible as they are small compared to the temperature rises associated with plastic deformation processes. Thus, the temperature error associated with sub-micron thickness coatings is acceptable. Combined with the TMM results shown in Fig. 4, a coating thickness of 250 nm of Titanium provides an opaque high emissivity coating that closely matches the specimen substrate thermal state. This specific coating was selected for experimental investigation.

2.3. Specimen preparation

Three specimens types with thicknesses of 3.175 mm with in plane dimensions as given in Fig. 6 were machined using waterjet cutting. Once waterjet cut, specimens for SHPB experiments required no further machining steps. Specimens used for IR detector calibration required the addition of a 0.5 mm diameter hole drilled 1 mm from the specimen surface (see Fig. 6(b). This hole allows for the insertion of a thermocouple to monitor temperature during IR detector calibration. Alignment specimens were designed to allow for the placement of a visible light source on their back side that would correspond with the position of the front surface interrogated by the IR detector during experimentation (see Fig. 6(c)).

Copper specimens were extracted from rolled sheet meeting ASTM F68 and Magnesium AZ31B specimens were extracted from rolled sheet meeting ASTM B90. Specimens were oriented such that their loading axis was aligned to the rolling principle processing direction. Once extracted, specimen surfaces were polished further using 180 grit silicon carbide abrasive paper to achieve a uniform surface finish across the materials investigated. Specimens were then cleaned with acetone, isopropanol, and DI water followed by oxygen plasma cleaning. Sputtering was conducted using a Denton Discovery 18 with a 99.995% purity Ti target. The pre-sputter time was set to 2 min followed by 19 min of sputtering with 100 W power. The base pressure was lowered to 1.9 μTorr and Ar pressure was set to 3 mTorr. A deposition rate of 13.08 nm/min was used to achieve a 250 nm thick opaque layer of Ti on the specimen surface.

2.4. Dynamic mechanical behavior characterization

High-strain rate deformation was accomplished using a tension split Hopkinson pressure bar (TSHPB). For more in depth discussion of TSHPB experimentation and signal analysis, the reader is encouraged to review Refs. [57,58]. The TSHPB setup used consists of a 3.658 m long incident and transmitted bars and a striker tube with a length of 457.2 mm, all made from 350C maraging-steel. At the mid-length position of the incident and transmitted bars, strain gauges are mounted in a full-Wheatstone bridge configuration to monitor propagating waves. The full bridge configuration has multiple advantages including higher signal-to-noise ratio, automatic cancelling of bending strains and Poisson effects, and compensates for lead wire resistance and temperature.

In a TSHPB experiment a striker tube is launched via gas gun impacting a flange on the end of an incident bar which generates a tensile stress wave that travels down the length of the incident bar towards a specimen. The specimen is mounted using a press fit collet system between the incident and transmitted bar. The collet system was purchased from REL Inc. (Calumet, MI). When the propagating tensile wave reaches the specimen, a portion of the wave is transmitted into the specimen, and a portion is reflected backwards towards the impacted flange. A portion of the wave passes through the specimen into the transmitted bar. A schematic of the TSHPB setup, the optical system, IR detector, and high speed camera system is presented in Fig. 7(a). Raw data traces recorded by the incident and transmitted bar mounted strain gauges and the IR detector output are shown in Fig. 7(b). Due to the significantly different amplitudes of each transducer, signals have been normalized by their respective magnitudes. Note, pulse shaping in the form of four semicircular copper pieces with 6.35 mm diameter and 0.5 mm thickness were placed 90 degrees apart on the flange to mechanically filter high frequency content out of the propagating wave pulses. Pulse shaping was used in all experiments thus dispersion correction was not utilized in the analysis due to the limited frequency content of propagating pulse.

Assuming one-dimensional wave propagation, strain gauge signals are reduced to obtain the sample's nominal strain rate, strain, and stress. The engineering strain rate of the specimen can be written as follows,

$$\dot{\epsilon}(t)_{spec} = -2\frac{c_0}{L_s}\epsilon_R(t), \tag{6}$$

where, $\dot{\epsilon}(t)_{spec}$ denotes the specimen's nominal strain rate, c_0 is the bar wave speed, L_s is the sample gauge length, and $\epsilon_R(t)$ is the reflective wave strain. Integrating the engineering strain rate over the loading pulse duration provides the engineering strain of the sample,

$$\epsilon_{spec}(t) = \int_0^t \dot{\epsilon}(\tau)d\tau. \tag{7}$$

The sample's nominal engineering stress $\sigma_{spec}(t)$ is obtained by

$$\sigma_{spec}(t) = \frac{A_{bar}E_{bar}\epsilon_T(t)}{t_{spec}w_{spec}} \tag{8}$$

where, A_{bar} is the cross-sectional area of the incident or transmitted bar, E_{bar} is the elastic modulus of the bars, $\epsilon_T(t)$ is the transmitted strain, and t_{spec}, w_{spec} are the thickness and width of the sample's gauge section respectively. Using the engineering strain and stress, the corresponding true strain, and stress can be found using:

$$\sigma_{true}(t) = \sigma_{spec}(t)[1 - \epsilon_{spec}(t)] \tag{9}$$

$$\epsilon_{true}(t) = ln[1 + \epsilon_{spec}(t)]. \tag{10}$$

The transient heat conduction equation, presented in Eq. (4), requires taking the time derivative of experimental data to obtain β_{diff}. Due to the sensitivity of time derivatives to experimental noise, the calculation and reporting of β_{int} is more common (see Fig. 1). Invoking the same assumptions of negligible thermo-elastic effects, and adiabatic conditions, the transient heat conduction equation simplifies to,

$$\beta_{int}(\epsilon, \dot{\epsilon}) = \frac{\rho c_p \Delta T}{\int dW_p} \tag{11}$$

where, c_p is heat capacity, ρ is density, ΔT is temperature rise, and W_p is plastic work. Due to the inability to directly measure low strain properties of materials using the TSHPB (e.g., elastic modulus and yield stress using a 0.2% strain offset) the denominator of Eq. (11) is approximated as the integral of the entire true stress–strain behavior. Furthermore, heat capacity values used when calculating β_{int} are approximated to be constant despite heat capacity being a temperature dependent property. This assumption is based on the limited temperature rises observed across experiments (≤ 15 °C).

Lastly, to assess the deposited 250 nm Ti coating robustness during deformation high speed imaging was conducted. A Shimadzu HPVX-2 camera was used to capture images of the entire loading duration at a frame rate of 333,333 fps.

2.5. IR detector calibration process

The optical system used to collect and direct IR radiation emitted by a deforming specimen has a double-Schwarzschild design. This optical system consists of two convex and concave gold-plated mirrors in series. Its design is presented in detail in Ref. [59]. Both concave mirrors have concentric holes with diameters equal to the diameter of the convex mirrors. Both Schwarzschild objectives operate at infinite conjugation ratio. The alignment procedure was guided by visible light. During the

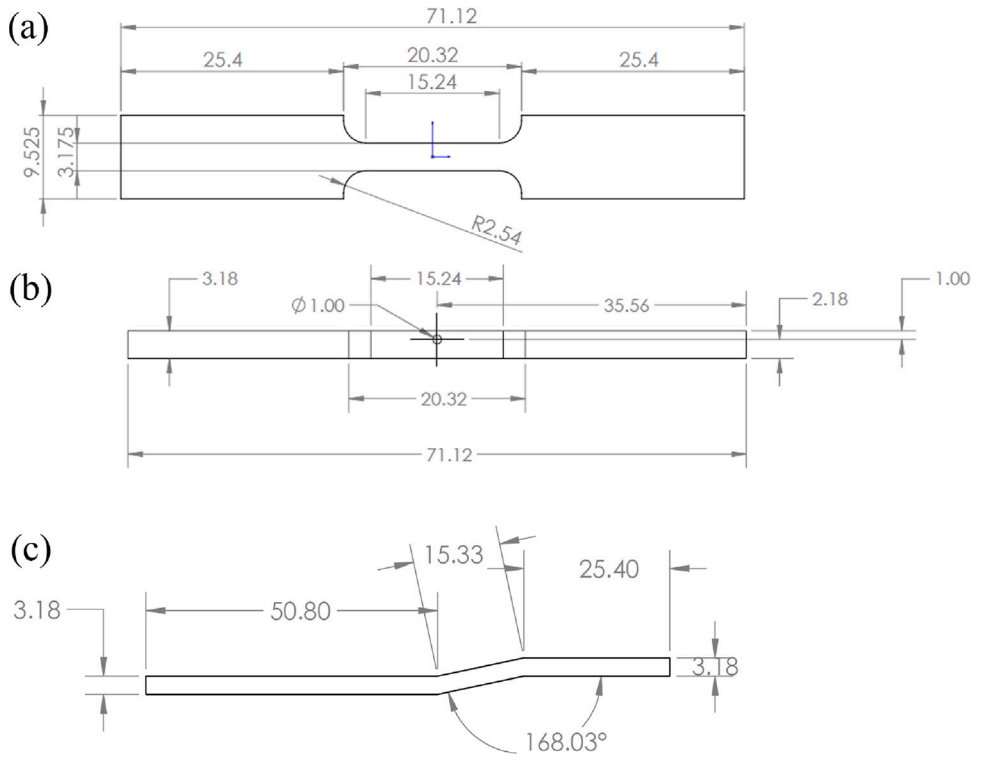

Fig. 6. Schematic of the (a) tension specimen, (b) calibration specimen, and (c) alignment specimen geometries used in IR thermography experiments, IR detector calibration, and optical system alignment, respectively. All dimensions in mm.

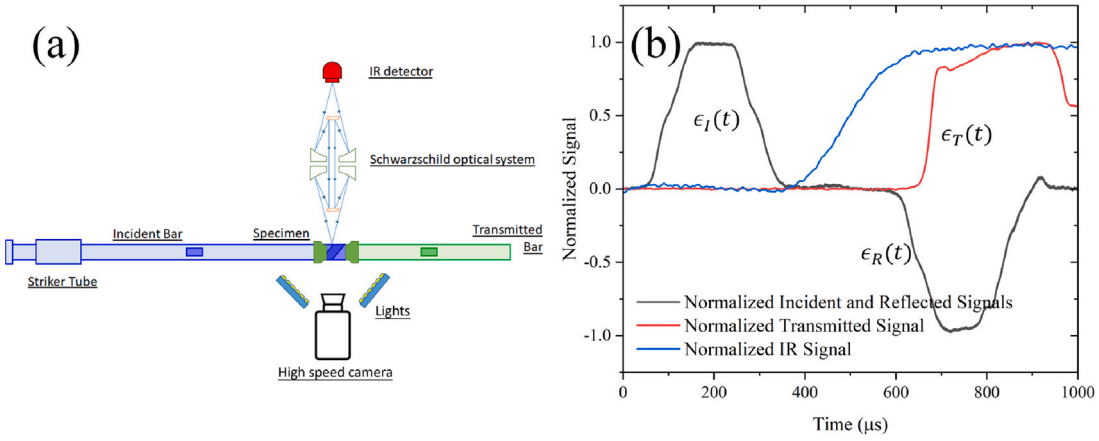

Fig. 7. (a) Experimental setup consisting of TSHPB, Schwarzschild optical system, IR detector, High speed camera. (b) Typical signal from TSHPB experiment.

alignment (and calibration process) the incident bar was brought into contact with a rigid stop to ensure consistent placement of specimen's relative to the IR detector and optical system. The alignment specimen matches the dimensions of a tension specimen and has a 0.5 mm hole drilled through the center of the gauge section to allow light to pass though. A strain gauge was placed on the surface of an alignment specimen and illuminated from the back side. The optical system was then focused to achieve a clear image of the strain gauge serpentine on the IR detector plane. Once aligned, the IR detector calibration process was conducted in accordance with the method presented by Hodowany et al. [60] and Nieto-Fuentes et al. [61].

The objective of the calibration process is to obtain the relationship between the recorded IR voltage and the specimen temperature. Since the liquid nitrogen cooled MCT HgCdTe IR detector's DC signals are blocked by an AC-coupling capacitor located in the pre-amplifier circuit, only dynamic temperature changes can be recorded by the IR detector [3]. Therefore, a chopping wheel made from copper was used to provide a dynamic signal for the IR detector. A K-type thermocouple with a 0.25 mm bead size was positioned inside the drilled hole of the calibration specimen to measure sub-surface temperature. The calibration specimen was heated using a high power soldering iron to temperatures exceeding those possible assuming a perfect conversion of all plastic work into heat of the specimen material ($\beta_{int} > 1$). Once the target temperature was exceeded, specimen cooling was recorded by the thermocouple. To check the validity of the thermocouple output, a resistance temperature detector (RTD) was bonded to the surface of the calibration specimen and the temperatures were recorded by these two sensors. The temperature evolutions recorded by the thermocouple and RTD are reported in Fig. 8. The agreement of the two sensors provides evidence that the sub-surface temperatures observed by the thermocouple, and the coating surface temperatures observed by the RTD are nominally identical.

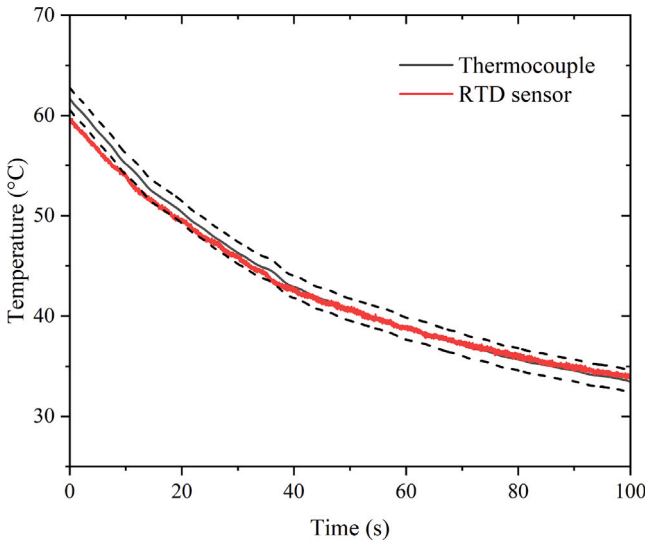

Fig. 8. Comparison of a surface RT measurement and embedded thermocouple temperature history during a calibration experiment. Dashed lines represent the temperature measurement uncertainty of the thermocouple.

3. Results and discussion

3.1. Calibration process

The two features of the selected sputter-deposited coating to be confirmed experimentally during the calibration process are (1) an increase of the emissivity of the coated specimen compared to the emissivity of the native specimen surface and (2) the coating is opaque. The results of the calibration process are shown in Fig. 9. In Fig. 9(a), the red, blue, and black dots show the voltage-temperature data obtained for Cu, Mg and Ti-coated Mg, respectively, from room temperature to 90° C. The decreased slope of the Ti-coated specimen compared to that of Cu and Mg, is a clear indication that there has been a substantial increase in the surface emissivity through the use of the Ti coating. Shown in Fig. 9(b), are the voltage-temperature calibration curves of Cu and Mg substrates each with a 250 nm thick Ti coating. The calibration curves fit to these data are nearly identical providing direct experimental evidence that the thickness predicted by TMM results in an opaque coating. Additionally, the close match of the calibration curves suggests that a single calibration curve can be applied across both the Cu and Mg substrate specimens.

Typically, in Taylor–Quinney coefficient investigations each specimen has a unique calibration curve. Thus, the results provided in Fig. 9 demonstrate the use of deposited coatings as a method to alleviate a known bottle neck in Taylor–Quinney coefficient investigations. Furthermore, the ability to reduce the number of calibration curves collected during a Taylor–Quinney coefficient investigation could aid in reducing lab-to-lab variation as calibration curves unique to each specimen would no longer be needed.

3.2. Copper TSHPB experiments

An additional feature of the deposited coating that must be demonstrated experimentally is that coated specimens provide consistent Taylor–Quinney coefficient values that are in agreement with previously reported data. Three experiments were conducted on coated Cu samples using the TSHPB. Fig. 10 shows the raw data traces captured during a TSHPB experiment where multiple wave reflections reload the specimen. As was demonstrated in Fig. 9 the native surface of Cu is significantly lower than that of the Ti-coated specimen. Therefore, if the coating changes thickness or the coating fails during the first or second loading of the specimen there would be a notable change in the slope of the IR detector signal as a function of time caused by a reduction in the specimen's emissivity. The constant slope following each loading increment of the specimen is a clear indication that the performance of the coating does not change over the levels of strain experienced by the specimen. Additionally, if present a change in slope between loading increments would indicate that the temperature of the coating does not match the thermal state of the underlying substrate. Thus the constant slope also points to the 250 nm thick coating matching the temperature of the deforming substrate.

The stress–strain behavior of the three Cu specimens deformed at a nominal strain rate of 935 s^{-1} is presented in Fig. 11(a). Specimens exhibited an approximate yield strength of 250 MPa followed by linear strain hardening. A strain of 16% was achieved for all specimens prior to unloading. At this level of strain no indication of necking was observed and deformation in the specimen gauge section can be assumed to be uniform. The true stress–strain behavior and temperature rise data are then used to calculate the plastic work to heat conversion (β_{int}) for each experiment. Material specific values of heat capacity and density used are 385 J/kg°C [56] and 8960 kg/m^3 [56], respectively. β_{int} is frequently reported as a single value determined by fitting a linear relationship to the slope of the temperature rise as a function of plastic work (see Fig. 11(b)) or as an evolving value that is dependent on strain (see Fig. 11(c)). In Figs. 11(b) and (c), the dashed lines surrounding the solid lines indicate the effect of the measurement uncertainty of the thermocouple used during the calibration step (±1.1 °C). It can be seen that across the replicate experiments values obtained are these values are repeatable and in agreement with each other. The fluctuations in the β_{int} coefficient at low strains should be expected. As has been mentioned previously, over the earliest stages of deformation the TSHPB cannot provide an accurate representation of the specimen mechanical behavior due to one-dimensional wave propagation assumptions taking multiple wave transits across the specimen to establish. Additionally, the thermoelastic effect is still present which causes temperature change of the specimen but these small values are unaccounted for during analysis.

Surveying literature finds a handful of modern investigations that have examined the Taylor–Quinney coefficient of Cu. The results of Rittel et al. [5] and Soares and Hokka [16] are included in Fig. 11 for comparison to the current work. Rittel et al. [5] examined the plastic work to heat conversion of single crystal and polycrystalline crystalline at low and high strain rates spanning 3000 to 8000 s^{-1} under compression. In their work a single average beta value was assigned based on the slope of the temperature rise as a function of plastic work density. Only the values obtained the lowest strain rate are included in Fig. 11(d). While the loading type and strain rates are different than those used in the current work, similar trends in results are observed. Both this study and the work of Rittel et al. [5] observed a linear relationship between work density and temperature rise. The presence of a linear relationship between work density and temperature rise also provides an indirect indication that the deposited coating remains intact throughout deformation. As was shown in Fig. 9, the emissivity of the copper surface is significantly lower than that of the coated surface. Had the Ti coating failed a non-linear relationship would be present in Fig. 11(b). Soares and Hokka [16] performed dynamic compression on polycrystalline copper over strain rates spanning 1300 to 3100 s^{-1}. Over the span they investigated it was determined that the evolution of the Taylor–Quinney coefficient was independent of strain rate. Comparing their results obtained at strain rate of 1300 s^{-1} finds them to be strong agreement with the values of obtained in the presented work for Ti-coated copper. The seminal work of Farren and Taylor, and Taylor and Quinney also investigated copper, reporting β values greater than those found here (0.905 to 0.92 [1] and 0.89 to 0.96 respectively [2]). Despite disagreement on the amplitude of β, there is agreement in that polycrystalline copper exhibits a nearly constant β throughout plastic deformation. Ultimately,

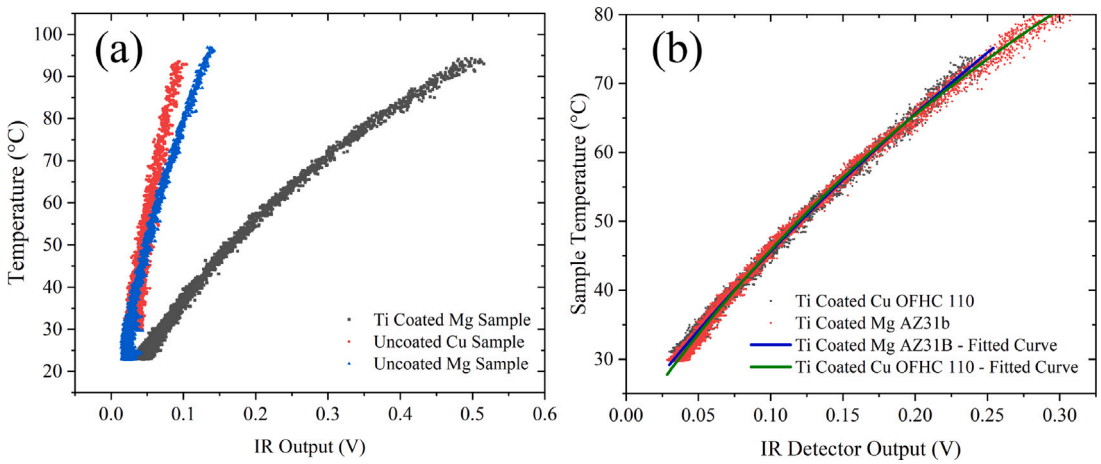

Fig. 9. Calibration curves for (a) native Cu and Mg surfaces compared to Ti-coated Mg and (b) a comparison of Ti coated Cu vs Ti coated Mg calibration curves.

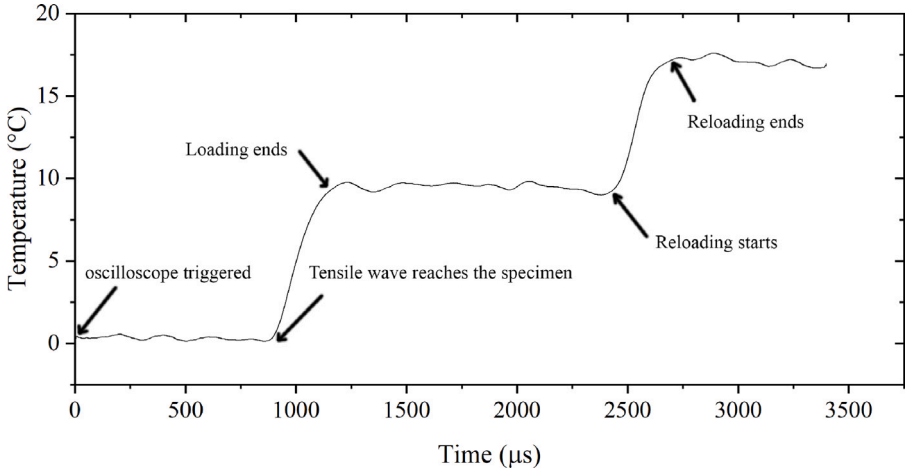

Fig. 10. Time–temperature rise history of a TSHPB experiment showing a uniform thermal state of the specimen between subsequent re-loading(s) caused by wave reflections in the SHPB.

the observation of trends that are in correspond between the Ti-coated Cu specimens and previous reports of Cu specimens provides further evidence that the 250 nm deposited Ti coating does not noticeably impact Taylor–Quinney coefficient quantification for copper.

3.3. Mg TSHPB experiments

An additional set of two experiments were conducted to examine the Taylor–Quinney behavior of Mg alloy AZ31B. Analysis steps are identical to those used for Cu and results are reported in Fig. 12. Material specific values used when calculating β_{int} for heat capacity and density used are 1000 J/kg°C [62] and 1754 kg/m^3 [62], respectively. Specimens exhibited an approximate yield strength of 400 MPa followed by linear strain hardening. As with copper a linear relationship was observed between temperature rise and work density.

To date, Taylor–Quinney studies of Mg and Mg alloys have focused on quantifying β_{int} under shear dominated loading conditions. This compounded with the hexagonal-close packed structure of Mg leads to challenges in drawing comparisons across previously reported Taylor–Quinney coefficients for Mg [17] and Mg alloys [17,22]. The strong crystallographic textures that develop during the processing of Mg result in orientation dependent mechanical behavior and the activation of dislocation slip and twinning mechanisms on different crystallographic planes that have dramatically different critical resolved shear stresses. As has been reported previously [22], the Taylor–Quinney coefficient is dependent on which mechanisms and to the extent they are activated. Additionally, a portion of previously reported work has focused on material states achieved after complex processing involving severe plastic deformation [17]. With the objective of the current work to investigate the use of thin coatings to improve signal quality without contaminating Taylor–Quinney coefficient measurement, the study of the contribution of specific mechanisms to the values obtained is outside of the current work's scope. However, general comparisons can be drawn with respect to the relative magnitude of values found here in to those captured from native Mg surfaces. In Fig. 12(c) the Taylor–Quinney coefficients reported for slip dominated deformation of AZ31B are included. It can be seen that the tensile loading Taylor–Quinney coefficients are comparable in magnitude to those reported for Mg and Mg alloys in literature.

3.4. Coating bonding

Results reported above rely on the assumption that the deposited coating remains intact during plastic deformation. Two methods are utilized to investigate the robust adhesion of between the Ti sputter deposited coating and the substrate. The first method utilizes in-situ high-speed imaging of the TSHPB experiment to visualize surface changes of the specimen and capture the presence of coating delamination or failure. The second method occurs post-mortem using energy dispersive x-ray spectroscopy (EDS) to confirm the amount of the coating coverage of the specimen surface that remains after the TSHPB experiment.

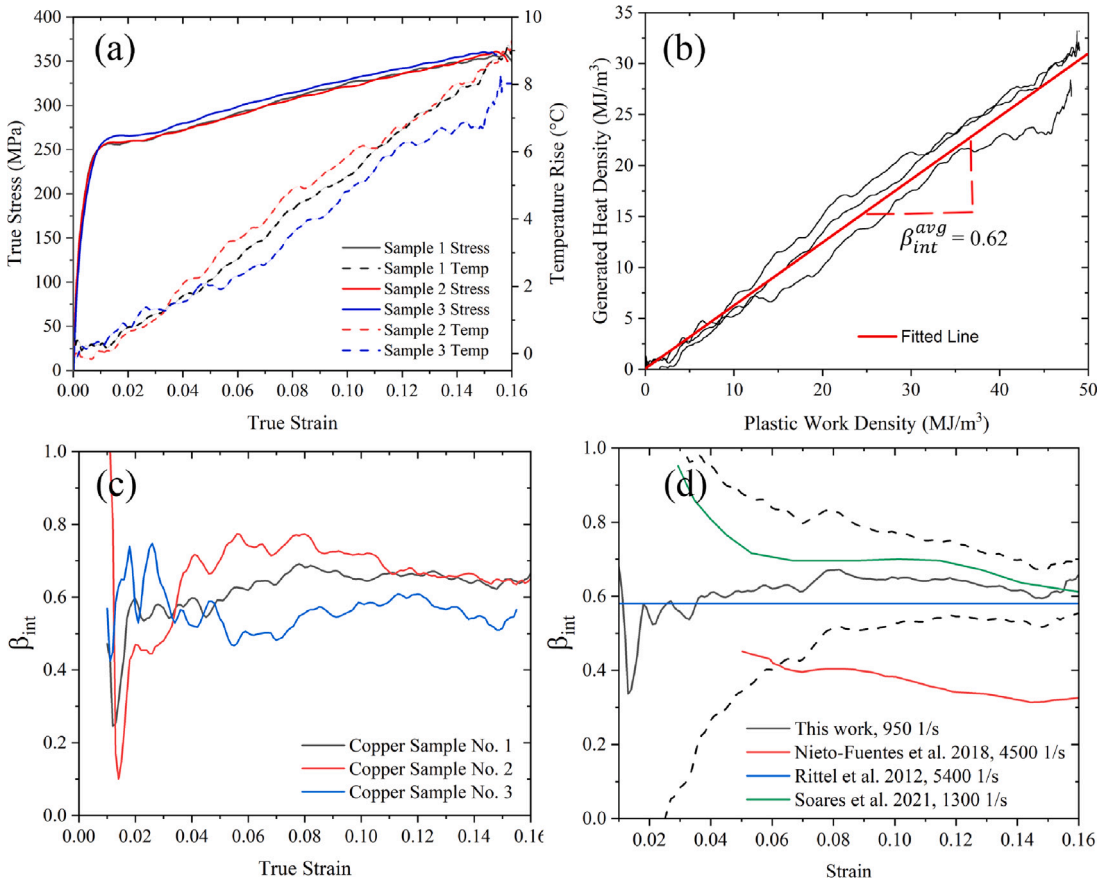

Fig. 11. (a) Triplicate Cu OFHC stress–strain curves obtained at a nominal strain rate of 935 s^{-1} and corresponding temperature rise, (b) evolution of temperature as a function of plastic work density, (c) Taylor–Quinney coefficients as a function of true strain for each specimen and (d) comparison of the average Taylor–Quinney coefficient evolution as a function of plastic strain with literature values [5,16,35].

Fig. 13 presents the evolution of the specimen surface as a function of time up to failure for a representative experiment. The increasing contrast as a function of time occurs due the increased surface roughness of the specimen in response to plastic deformation. It is clear that although the specimen surface roughness increases, debonding, or delamination of the deposited coating does not occur even up to fracture.

Post-mortem scanning electron microscopy and EDS analysis was conducted using a Teneo SEM equipped with a EDAX detector on Mg and Cu specimens. EDS analysis was limited to regions of homogeneous deformation where the state of strain could be approximated. Representative SEM and EDS results of an Mg specimen is shown in Fig. 14. All Mg specimens failed during a single loading increment (as was shown in Fig. 13) and represents the damage state of the coating at 10% strain. The secondary electron image shows the coating surface with limited regions of cracking and no evidence of debonding or delamination. EDS analysis of the elemental composition of the post-experiment surface conducted over the indicated region in Fig. 13(a) provides a clear indication that the coating remains intact and there are limited regions where the substrate is visible. A surface area analysis finds that the coating remains over 96% of the scanned area surface.

Cu specimens examined were subjected to multiple reloadings due the purposeful omission of momentum trapping in the TSHPB experiment. The omission of a momentum trap was motivated by multiple reloadings being likely to result in the coating having a damage state that exceeds that exhibited during the first loading cycle during which the Taylor–Quinney coefficient is determined. The damage state of the coating will be influenced both by an increase of accumulated strain, but also by inertial effects encouraging delamination of regions of the coating damaged during a previous loading increment. The coating state of the Cu specimen represents the damage state of the coating at 40% strain which is more than twice the strain level of Taylor–Quinney coefficient values reported above.

In Fig. 15 a secondary electron image and EDS element map are provided. The secondary electron images shows substantial break up of the surface coating. The EDS analysis map also provides a clear indication that the coating has been damaged during the multiple reloading steps of a non-momentum trapped TSHPB experiment. Surface area analysis of EDS data indicates that 69% of the surface remains covered by the Ti-coating.

3.5. Strain limitations when using high emissivity coatings

As the surface area of the exposed substrate increases this will have an impact on the obtained IR detector output. For the Cu and Mg substrate cases examined with a high emissivity Ti coating, the calculated specimen temperature will be over reported due to the lower emissivity of the exposed substrate. A simple strain dependent rule of mixtures modification of Eq. (3) is proposed in Eq. (12) to estimate the effect of the exposed substrate material on IR detector performance, and to assess the limitations of the strain levels that can be investigated using the proposed coating technique,

$$\zeta(T)_{tot} = C_0 \left[A(\varepsilon)_s \int_{\lambda_1}^{\lambda_2} B(T,\lambda)\epsilon_s(\lambda)\chi(\lambda)\,d\lambda + A(\varepsilon)_c \int_{\lambda_1}^{\lambda_2} B(T,\lambda)\epsilon_c(\lambda)\chi(\lambda)\,d\lambda \right] \tag{12}$$

where, the subscripts s and c indicate the substrate and coating respectively, and $A(\varepsilon)$ is the strain dependent surface coating area percentage

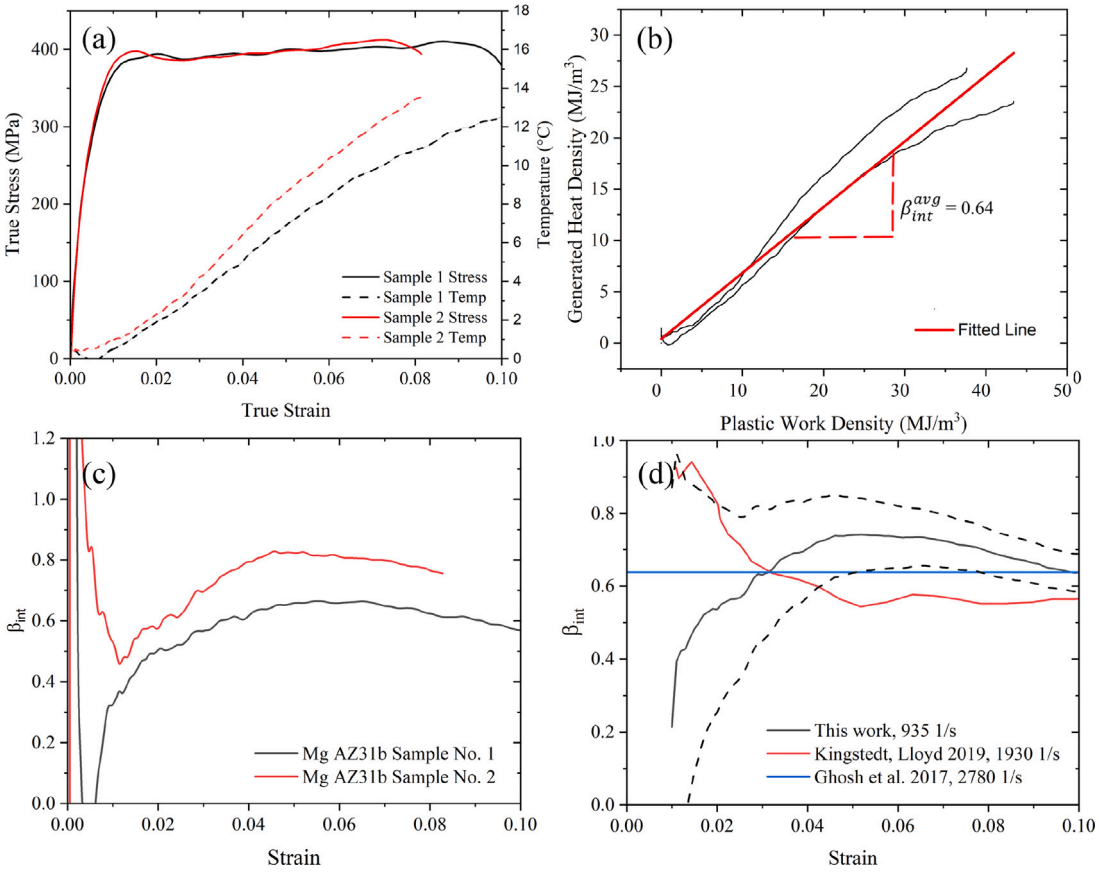

Fig. 12. (a) Triplicate Mg AZ31b stress–strain curves obtained at a strain rate of 935 s^{-1} and corresponding temperature rise, (b) evolution of temperature as a function of plastic work density, (c) Taylor–Quinney coefficients as a function of true strain for each specimen and (d) Comparison of Taylor–Quinney coefficients with literature [17,22].

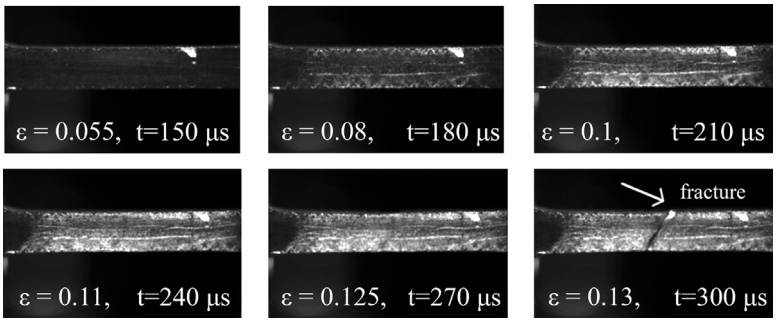

Fig. 13. Mg AZ31B High speed imaging.

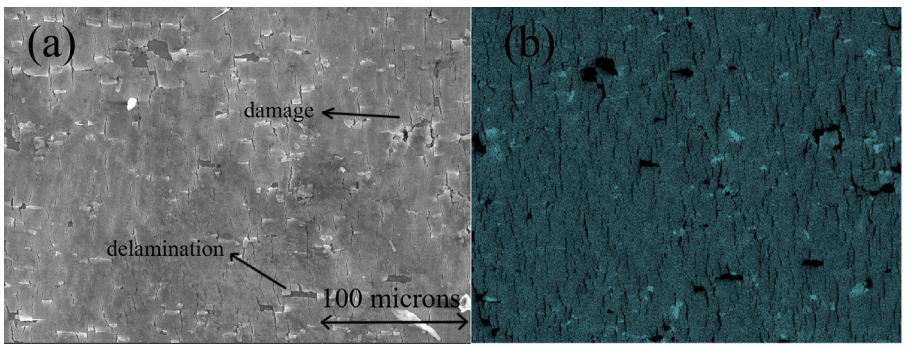

Fig. 14. Post-mortem analysis of Ti coated Mg AZ31B a) Secondary electron image from the surface of the deformed sample (b) EDS map of Ti-K emissions from the surface of the sample showing the Ti coating layer.

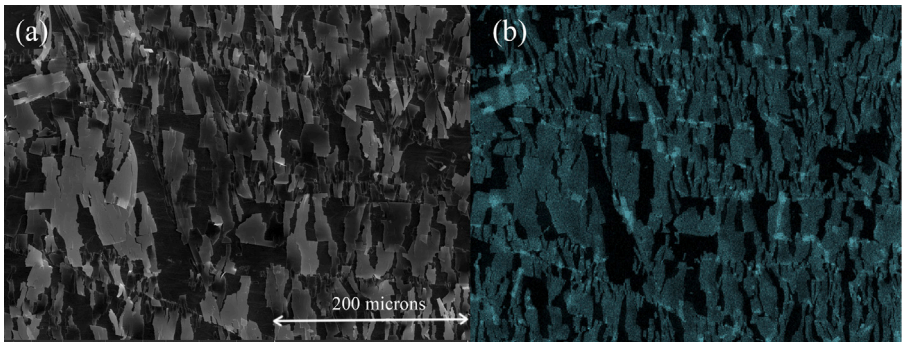

Fig. 15. Post-mortem analysis of Ti coated Cu OFHC 110 (a) Secondary electron image from the surface of the deformed sample (b) EDS map of Ti-K emissions from the surface of the sample showing the Ti coating layer.

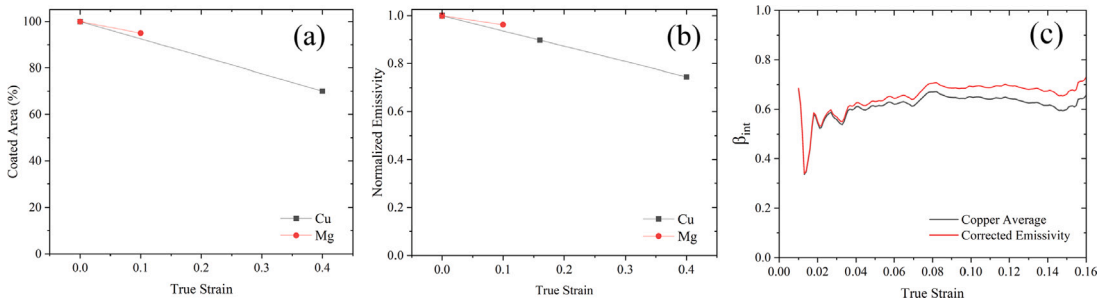

Fig. 16. Overview of the strain dependent changes in (a) coated surface area, (b) emissivity change, and (c) impact on the reported Taylor–Quinney coefficient.

shown in Fig. 16(a). In Fig. 16(b), the specimen emissivity using the strain dependent rule of mixtures is reported. Considering the SHPB has a reported stress–strain measurement of uncertainty of 4% [63] the small emissivity change of the coated of Mg specimens up to failure is not likely to meaningfully impact results. Conversely, the coating degradation that accumulates of up 40% strain in the copper specimens should not be ignored. Shown in Fig. 16 is the impact of the linear emissivity change on the reported Taylor–Quinney coefficient for copper. The change in coated surface area decreases the average surface emissivity due to Mg and Cu having a lower emissivity than the deposited Ti coating. The Taylor–Quinney coefficient is corrected based on the emissivity change and reported in Fig. 16(c). It can be observed that the emissivity decrease caused by the coating delamination has a limited impact on the Taylor–Quinney coefficient with changes the total change being less than the experiment-to-experiment variation measured in the current work (see Fig. 11(c))

4. Conclusions and summary

A coating design process motivated by the desire to increase signal to noise ratio, and thereby provide a means to reduce lab-to-lab variability in the measurement of temperature rise during adiabatic high-strain rate infra-red (IR) thermography experiments is introduced. Electromagnetic aspects of common sputter deposition sources were investigated using a validated TMM code, and heat transfer aspects of coatings were modeling using finite elements to identify a 250 nm thick Ti coating as a promising candidate to improve surface emissivity of Cu and Mg AZ31B substrates. Coating substrates were found to have a four to six times improvement in surface emissivity as well as coating specimens were determined to have nominally identical calibration curves. Taylor–Quinney coefficients obtained from coated specimens were compared to previously reported values and were found to be in general agreement. Post-mortem electron microscopy analysis and high-speed imaging confirm robust adhesion between the sputtered Ti layer and the metallic substrate material system during high-strain rate deformation.

From a practical standpoint the current work provides an economical approach to (1) reduce a known source of uncertainty in Taylor–Quinney coefficient measurement, specifically in enabling the use of a single calibration curve for coated materials regardless of the specimen substrate, (2) remove the need to obtain specimen specific calibration curves, and (3) improve signal-to-noise ratios during the earliest stages of deformation through specimen failure. While the approaches shown here are demonstrated using a split-Hopkinson tension bar, they can be translated for use on a split-Hopkinson pressure bar. Ultimately, the proposed approach could provide a homogenization and simplification of approach to what has traditionally be a challenging experimental mechanics problem to address.

CRediT authorship contribution statement

Seyyed-Danial Salehi: Investigation, Formal analysis, Methodology, Writing – original draft, Writing – review & editing, Visualization. **Owen Kingstedt:** Methodology, Resources, Supervision, Writing – original draft, Writing – review & editing.

Declaration of competing interest

The authors declare that they have no known competing financial interests or personal relationships that could have appeared to influence the work reported in this paper.

Data availability

Data will be made available on request.

Acknowledgments

This research was supported by the National Science Foundation, United States CAREER award no. 1847653. A portion of the presented work made use of University of Utah shared facilities of the Micron Technology Foundation Inc. Microscopy Suite sponsored by the College

of Engineering, Health Sciences Center, Office of the Vice President for Research, and the Utah Science Technology and Research (USTAR) initiative of the State of Utah. The authors would like to thank Dr. Paulo Perez and Dr. Brian Van Devener from surface analysis lab at Utah nanofab for their assistance in equipment operation and training. Additionally, a portion of this work was performed in part at the Utah Nanofab sponsored by the College of Engineering, Office of the Vice President for Research, and the Utah Science Technology and Research (USTAR) initiative of the State of Utah. The author(s) appreciate the support of the staff and facilities that made this work possible. The help of Mr. Eric Fluckiger, and Mr. Andrew Hurlbut at Utah Nanofab for sample preparation is also greatly acknowledged.

Appendix A. Supplementary data

Supplementary material related to this article can be found online at https://doi.org/10.1016/j.ijimpeng.2023.104593.

References

[1] Farren WS, Taylor GI. The heat developed during plastic extension of metals. Proc R Soc Lond Ser A 1925;107(743):422–51.
[2] Taylor GI, Quinney H. The latent energy remaining in a metal after cold working. Proc R Soc Lond Ser A 1934;143(849):307–26.
[3] Hodowany J, Ravichandran G, Rosakis A, Rosakis P. Partition of plastic work into heat and stored energy in metals. Exp Mech 2000;40(2):113–23.
[4] Bever MB, Holt DL, Titchener AL. The stored energy of cold work. Prog Mater Sci 1973;17:5–177.
[5] Rittel D, Kidane A, Alkhader M, Venkert A, Landau P, Ravichandran G. On the dynamically stored energy of cold work in pure single crystal and polycrystalline copper. Acta Mater 2012;60(9):3719–28.
[6] Guzmán R, Meléndez J, Zahr J, Pérez-Castellanos J. Determination of the constitutive relation parameters of a metallic material by measurement of temperature increment in compressive dynamic tests. Exp Mech 2010;50(3):389–97.
[7] Zhang T, Jiao Z, Wang Z, Qiao J. Dynamic deformation behaviors and constitutive relations of an AlCoCr1. 5Fe1. 5NiTi0. 5 high-entropy alloy. Scr Mater 2017;136:15–9.
[8] Meyer L, Herzig N, Halle T, Hahn F, Krueger L, Staudhammer K. A basic approach for strain rate dependent energy conversion including heat transfer effects: an experimental and numerical study. J Mater Process Technol 2007;182(1–3):319–26.
[9] Song B, Sanborn B. A modified Johnson–Cook model for dynamic response of metals with an explicit strain-and strain-rate-dependent adiabatic thermosoftening effect. J Dyn Behav Mater 2019;5(3):212–20.
[10] Clifton R, Duffy J, Hartley K, Shawki T. On critical conditions for shear band formation at high strain rates. Tech. rep., Brown Univ Providence Ri Div of Engineering; 1984.
[11] Rittel D, Wang Z, Merzer M. Adiabatic shear failure and dynamic stored energy of cold work. Phys Rev Lett 2006;96(7):075502.
[12] Zehnder AT, Rosakis AJ. On the temperature distribution at the vicinity of dynamically propagating cracks in 4340 steel. J Mech Phys Solids 1991;39(3):385–415.
[13] Kallivayalil JA, Zehnder AT. Measurement of the temperature field induced by dynamic crack growth in Beta-C titanium. Int J Fract 1994;66(2):99–120.
[14] Zhou M, Rosakis A, Ravichandran G. Dynamically propagating shear bands in impact-loaded prenotched plates—I. Experimental investigations of temperature signatures and propagation speed. J Mech Phys Solids 1996;44(6):981–1006.
[15] Mason J, Rosakis A, Ravichandran G. On the strain and strain rate dependence of the fraction of plastic work converted to heat: an experimental study using high speed infrared detectors and the Kolsky bar. Mech Mater 1994;17(2–3):135–45.
[16] Soares G, Hokka M. The Taylor–Quinney coefficients and strain hardening of commercially pure titanium, iron, copper, and tin in high rate compression. Int J Impact Eng 2021;156:103940.
[17] Ghosh D, Kingstedt OT, Ravichandran G. Plastic work to heat conversion during high-strain rate deformation of Mg and Mg alloy. Metall Mater Trans A 2017;48(1):14–9.
[18] Rittel D, Zhang L, Osovski S. The dependence of the Taylor–Quinney coefficient on the dynamic loading mode. J Mech Phys Solids 2017;107:96–114.
[19] Oliferuk W, Korbel A, Grabski MW. Mode of deformation and the rate of energy storage during uniaxial tensile deformation of austenitic steel. Mater Sci Eng A 1996;220(1–2):123–8.
[20] Williams R. The stored energy in deformed copper: the effect of grain size and silver content. Acta Metall 1961;9(10):949–57.
[21] Varga J, Kingstedt OT. An investigation of the plastic work to heat conversion of wrought and laser powder bed fusion manufactured Inconel 718. Addit Manuf 2021;46:102179.
[22] Kingstedt OT, Lloyd JT. On the conversion of plastic work to heat in Mg alloy AZ31B for dislocation slip and twinning deformation. Mech Mater 2019;134:176–84.
[23] Rittel D. On the conversion of plastic work to heat during high strain rate deformation of glassy polymers. Mech Mater 1999;31(2):131–9.
[24] Guo Y, Ruan Q, Zhu S, Wei Q, Lu J, Hu B, et al. Dynamic failure of titanium: Temperature rise and adiabatic shear band formation. J Mech Phys Solids 2020;135:103811.
[25] Zhang L, Rittel D, Osovski S. Thermo-mechanical characterization and dynamic failure of near α and near β titanium alloys. Mater Sci Eng A 2018;729:94–101.
[26] Macdougall D, Harding J. The measurement of specimen surface temperature in high-speed tension and torsion tests. Int J Impact Eng 1998;21(6):473–88.
[27] Macdougall D. Materials testing for constitutive relations (Ph.D. thesis), 1997.
[28] Nieto-Fuentes J, Osovski S, Venkert A, Rittel D. Reassessment of the dynamic thermomechanical conversion in metals. Phys Rev Lett 2019;123(25):255502.
[29] Smith JL. Full-field measurement of the Taylor–Quinney coefficient in tension tests of Ti-6Al-4V, aluminum 2024-T351, and inconel 718 at various strain rates (Ph.D. thesis), 2019, p. 109.
[30] Jovic C, Wagner D, Herve P, Gary G, Lazzarotto L. Mechanical behaviour and temperature measurement during dynamic deformation on split Hopkinson bar of 304L stainless steel and 5754 aluminium alloy. J Physique IV (Proc) 2006;134:1279–85.
[31] Vazquez-Fernandez N, Soares G, Smith J, Seidt J, Isakov M, Gilat A, et al. Adiabatic heating of austenitic stainless steels at different strain rates. J Dyn Behav Mater 2019;5(3):221–9.
[32] Kapoor R, Nemat-Nasser S. Determination of temperature rise during high strain rate deformation. Mech Mater 1998;27(1):1–12.
[33] Vernaza-Pena K, Mason J, Li M. Experimental study of the temperature field generated during orthogonal machining of an aluminum alloy. Exp Mech 2002;42(2):221–9.
[34] Ravichandran G, Rosakis AJ, Hodowany J, Rosakis P. On the conversion of plastic work into heat during high-strain-rate deformation. In: AIP conference proceedings, vol. 620, no. 1. American Institute of Physics; 2002, p. 557–62.
[35] Nieto-Fuentes J, Rittel D, Osovski S. On a dislocation-based constitutive model and dynamic thermomechanical considerations. Int J Plast 2018;108:55–69.
[36] Guduru P, Rosakis A, Ravichandran G. Dynamic shear bands: an investigation using high speed optical and infrared diagnostics. Mech Mater 2001;33(7):371–402.
[37] Zehnder AT, Guduru PR, Rosakis AJ, Ravichandran G. Million frames per second infrared imaging system. Rev Sci Instrum 2000;71(10):3762–8.
[38] He X, Li Y, Wang L, Sun Y, Zhang S. High emissivity coatings for high temperature application: progress and prospect. Thin Solid Films 2009;517(17):5120–9.
[39] Shimazaki K, Imaizumi M, Kibe K. SiO2 and Al2O3/SiO2 coatings for increasing emissivity of Cu (In, Ga) Se2 thin-film solar cells for space applications. Thin Solid Films 2008;516(8):2218–24.
[40] Falz M, Leonhardt G. PVD coatings with high IR emissivity for high temperature applications of Co-based alloys. Surf Coat Technol 1993;61(1–3):97–100.
[41] Tang H, Xin T, Sun Q, Yi C, Jiang Z, Wang F. Influence of FeSO4 concentration on thermal emissivity of coatings formed on titanium alloy by micro-arc oxidation. Appl Surf Sci 2011;257(24):10839–44.
[42] Tang H, Sun Q, Xin T, Yi C, Jiang Z, Wang F. Influence of Co (CH3coo) 2 concentration on thermal emissivity of coatings formed on titanium alloy by micro-arc oxidation. Curr Appl Phys 2012;12(1):284–90.
[43] Neuer G, Jaroma-Weiland G. Spectral and total emissivity of high-temperature materials. Int J Thermophys 1998;19(3):917–29.
[44] Ordal MA, Bell RJ, Alexander RW, Long LL, Querry MR. Optical properties of fourteen metals in the infrared and far infrared: Al, Co, Cu, Au, Fe, Pb, Mo, Ni, Pd, Pt, Ag, Ti, V, and W. Appl Opt 1985;24(24):4493–9.
[45] Hagemann H-J, Gudat W, Kunz C. Optical constants from the far infrared to the x-ray region: Mg, Al, Cu, Ag, Au, Bi, C, and Al 2 O 3. J Opt Soc Amer 1975;65(6):742–4.
[46] Wen C-D, Mudawar I. Modeling the effects of surface roughness on the emissivity of aluminum alloys. Int J Heat Mass Transfer 2006;49(23–24):4279–89.
[47] Konz W, Hildenbrand J, Bauersfeld M, Hartwig S, Lambrecht A, Lehmann V, et al. Micromachined IR-source with excellent blackbody like behaviour. In: Smart sensors, actuators, and MEMS II, vol. 5836. International Society for Optics and Photonics; 2005, p. 540–8.
[48] Lin S-Y, Moreno J, Fleming J. Three-dimensional photonic-crystal emitter for thermal photovoltaic power generation. Appl Phys Lett 2003;83(2):380–2.
[49] Kocer H, Butun S, Li Z, Aydin K. Reduced near-infrared absorption using ultra-thin lossy metals in Fabry–Perot cavities. Sci Rep 2015;5(1):1–6.
[50] Khorrami Y, Fathi D, Khavasi A, Rumpf RC. From asymmetrical to the nonreciprocal isolator using time-varying metasurfaces. 2021.
[51] Rumpf RC. Improved formulation of scattering matrices for semi-analytical methods that is consistent with convention. Prog Electromagn Res B 2011;35:241–61.
[52] Palik ED. Handbook of optical constants of solids, vol. 3. Academic Press; 1998.
[53] Rosakis P, Rosakis A, Ravichandran G, Hodowany J. A thermodynamic internal variable model for the partition of plastic work into heat and stored energy in metals. J Mech Phys Solids 2000;48(3):581–607.

[54] Zehnder A, Babinsky E, Palmer T. Hybrid method for determining the fraction of plastic work converted to heat. Exp Mech 1998;38(4):295–302.
[55] Hust JG, Lankford AB. Thermal conductivity of aluminum, copper, iron, and tungsten for temperatures from 1 K to the melting point. Tech.rep., National Bureau of Standards, Boulder, CO (USA). Chemical Engineering ...; 1984.
[56] Bauccio M, et al. ASM metals reference book. ASM international; 1993.
[57] Gama BA, Lopatnikov SL, Gillespie Jr JW. Hopkinson bar experimental technique: a critical review. Appl Mech Rev 2004;57(4):223–50.
[58] Chen WW, Song B. Split Hopkinson (Kolsky) bar: Design, testing and applications. Springer Science & Business Media; 2010.
[59] Salehi S-D, Beal R, Kingstedt OT. Dynamic behavior and thermomechanical characterization of laser powder bed fusion and wrought Ti-6Al-4V. Int. J. Impact Eng. 2023;104552.
[60] Hodowany J. On the conversion of plastic work into heat. California Institute of Technology; 1997.
[61] Nieto-Fuentes J, Osovski S, Rittel D. High-speed infrared thermal measurements of impacted metallic solids. MethodsX 2020;7:100914.
[62] Lee S, Ham HJ, Kwon SY, Kim SW, Suh CM. Thermal conductivity of magnesium alloys in the temperature range from- 125 C to 400 C. Int J Thermophys 2013;34(12):2343–50.
[63] Brizard D, Ronel S, Jacquelin E. Estimating measurement uncertainty on stress-strain curves from SHPB. Exp Mech 2017;57(5):735–42.